

**OPEN ACCESS**

# Lithium Redistribution Mechanism within Silicon-Graphite Electrodes: Multi-Method Approach and Method Validation

To cite this article: Christin Hogrefe *et al* 2024 *J. Electrochem. Soc.* **171** 070503

View the [article online](#) for updates and enhancements.

## You may also like

- [Comparison of acrylic polymer adhesive tapes and silicone optical grease in light sharing detectors for positron emission tomography](#)  
Devin J Van Elburg, Scott D Noble, Simone Hagey et al.
- [Particle-Level Modeling of the Charge-Discharge Behavior of Nanoparticulate Phase-Separating Li-Ion Battery Electrodes](#)  
Bernardo Orvananos, Todd R. Ferguson, Hui-Chia Yu et al.
- [Morphological Changes of Silicon Nanoparticles and the Influence of Cutoff Potentials in Silicon-Graphite Electrodes](#)  
Morten Wetjen, Sophie Solchenbach, Daniel Pritzl et al.



# Lithium Redistribution Mechanism within Silicon-Graphite Electrodes: Multi-Method Approach and Method Validation

Christin Hogrefe,<sup>1</sup> Neelima Paul,<sup>2</sup> Lioba Boveleth,<sup>3,4</sup> Marius Bolsinger,<sup>5</sup> Marius Flügel,<sup>1</sup> Timo Danner,<sup>3,4</sup> Arnulf Latz,<sup>3,4,6</sup> Ralph Gilles,<sup>2</sup> Volker Knoblauch,<sup>5</sup> Margret Wohlfahrt-Mehrens,<sup>1,4</sup> Markus Hölzle,<sup>1</sup> and Thomas Waldmann<sup>1,4,\*</sup>

<sup>1</sup>Zentrum für Sonnenenergie- und Wasserstoff-Forschung Baden-Württemberg, D-89081 Ulm, Germany

<sup>2</sup>Heinz Maier-Leibnitz Zentrum, Technische Universität München, D-85747 Garching, Germany

<sup>3</sup>German Aerospace Center, Institute of Engineering Thermodynamics, D-70569 Stuttgart, Germany

<sup>4</sup>Helmholtz Institute for Electrochemical Energy Storage, D-89081 Ulm, Germany

<sup>5</sup>Aalen University of Applied Sciences, Materials Research Institute, D-73430 Aalen, Germany

<sup>6</sup>Ulm University, Institute of Electrochemistry, D-89081 Ulm, Germany

Li redistribution processes within Si-graphite composite (SiG) electrodes are analyzed using in situ and operando X-ray diffraction (XRD), ex situ light microscopy (LM), in situ optical microscopy of cross-sectioned full cells (CS-IOM), and 3D microstructure-resolved simulations of full cells. First, the lithiation behavior of graphite and SiG full cells (Si content 20.8 wt.-%) is analyzed. The results are used as validation of the methods (XRD, LM, CS-IOM, simulation). Second, the Li redistribution between the graphite component and Si component within SiG electrodes is investigated: By operando XRD measurements during charging in comparison with relaxed cells, a higher lithiation degree in the graphite component is found during charging compared to the relaxed state, indicating Li redistribution from graphite to Si during relaxation. The Li redistribution is directly observed by in situ and ex situ optical microscopy, where the golden LiC<sub>6</sub> phase disappears during a 24 h relaxation period. The results are supported by simulations showing the variation in the Li concentration, not only in graphite but also within the Si component. Furthermore, all methods find that the Li redistribution is more pronounced at a higher C-rate of 0.5 C, suggesting a preference for graphite lithiation over Si lithiation.

© 2024 The Author(s). Published on behalf of The Electrochemical Society by IOP Publishing Limited. This is an open access article distributed under the terms of the Creative Commons Attribution 4.0 License (CC BY, <http://creativecommons.org/licenses/by/4.0/>), which permits unrestricted reuse of the work in any medium, provided the original work is properly cited. [DOI: 10.1149/1945-7111/ad59c7]



Manuscript submitted February 14, 2024; revised manuscript received May 8, 2024. Published July 3, 2024.

Supplementary material for this article is available [online](#)

In next generation Lithium-ion battery (LIB) cells, one way to increase the energy density of the batteries is mixing Si with graphite in the anodes.<sup>1</sup> Although Si has a theoretical capacity of 3,579 mAh g<sup>-1</sup> at room temperature (Li<sub>15</sub>Si<sub>4</sub>),<sup>2</sup> its useable capacity is mostly limited due to substantial expansion during lithiation (>300%) that results in various aging mechanisms related to Si anodes.<sup>2-5</sup> Additionally, the low electronic and diffusion coefficients of Li in Si (Electronic conductivity: 10<sup>-3</sup> S cm<sup>-1</sup>,<sup>6,7</sup> D<sub>Li+</sub>: 10<sup>-13</sup>-10<sup>-14</sup> cm<sup>2</sup> s<sup>-1</sup>)<sup>8-11</sup> compared to graphite (Electronic conductivity: 10<sup>4</sup> S cm<sup>-1</sup>,<sup>6,12</sup> D<sub>Li+</sub>: 10<sup>-8</sup>-10<sup>-12</sup> cm<sup>2</sup> s<sup>-1</sup>)<sup>13,14</sup> further limit the practical use of pure Si anodes.<sup>6</sup> By combining Si with graphite-based anode active material, the resulting Si-graphite blended and composite electrodes (SiG) allow utilization of the advantages of both materials: stability and electronic conductivity from the graphite combined with high capacity from Si, and therefore overall enhancing the performance of Si containing batteries.<sup>15</sup>

The formation of lithiated phases in both graphite and Si can be studied with various methods: X-ray diffraction (XRD) has been used extensively to study Li-graphite intercalation compounds (Li-GICs) in pure graphite electrodes.<sup>16-18</sup> In 1991, Dahn applied in situ XRD to determine the phase diagram for the electrochemical lithiation of graphite.<sup>16</sup> Li-GICs are also known to exhibit optically observable colors, with LiC<sub>18</sub> appearing blue,<sup>19,20</sup> LiC<sub>12</sub> appearing red,<sup>19,20</sup> and LiC<sub>6</sub> appearing yellow/gold.<sup>19</sup> These colors have been utilized for visual detection of lithiation fronts<sup>21-24</sup> and strains<sup>25</sup> in different kinds of optical cells. Optical measurements were primarily used for monitoring the expansion of the electrode material in Si-containing anodes.<sup>26,27</sup>

In different operando X-ray studies, it was found that SiG electrodes display asymmetric lithiation and de-lithiation behavior.<sup>28-30</sup> Yao et al.<sup>29</sup> used graphite and SiG (15 wt-% Si)

half cells in operando XRD measurements to determine the cell capacity contribution of Si in the SiG electrodes. Simultaneous recording of wide-angle X-ray scattering (WAXS) and small-angle X-ray scattering (SAXS) enabled Berhaut et al.<sup>30</sup> to monitor the respective contributions of the Si and graphite component to the cell capacity in pouch cells. The two studies revealed that during lithiation of SiG electrodes, Li is inserted into both components in parallel, while during delithiation, Li is mostly first extracted from graphite followed by Si.<sup>29,30</sup>

Physicochemical modeling allowed to unveil the competition of the different components during lithiation at different C-rates and loadings by quantifying the state-of-charge (SOC) in every part of the composite electrode.<sup>31,32</sup> The Li concentration in discretization compartments of the active materials is calculated and normalized by the maximum Li concentration of the respective material yielding a lithiation fraction comparable to the concept of SOC.<sup>32,33</sup> Therefore, modeling enables differentiation not only between the active materials but also between the exact positions within the electrode (e.g. surface or bulk) when analyzing the lithiation fraction. Such models are primarily based on measurable material parameters and reproduce the complexity of the electrochemical device in an ideal setting. The recently applied models for simulations of Si-containing electrodes focus on different scales, electrochemical-mechanical coupling, or higher computational efficiency, but either way show the interaction between Si and graphite by treating them as separate components.<sup>31,34-36</sup> These models reproduce the aforesaid experimental findings by showing, inter alia, the detailed concentration distribution with high spatial resolution which is not easily measurable.

Due to the different kinetic and thermodynamic properties of the individual components in blended or composite electrodes, a so-called "buffer-effect" can be observed where one component may be charged preferentially under specific conditions (e.g. high current pulses).<sup>37,38</sup> Consequently, this results in inhomogeneous charge distribution in the individual components. This effect has not been extensively studied in blended and composite SiG anodes so far.

\*Electrochemical Society Member.

<sup>z</sup>E-mail: [thomas.waldmann@zsw-bw.de](mailto:thomas.waldmann@zsw-bw.de)

For delithiation of composite anodes in a half cell, Finegan et al.<sup>39</sup> found by in situ high-energy X-ray diffraction computed tomography that Li redistribution occurred between Si and graphite during the relaxation period after charging pulses were applied due to crossover in the respective electrochemical potentials. Moon et al.<sup>40</sup> observed the direction of Li redistribution from Si to graphite during CV charging by using operando XRD and X-ray absorption fine structure (XAFS) spectroscopy for full cells with a SiG anode. In an operando neutron diffraction study conducted by Richter et al.,<sup>41</sup> the redistribution of Li from graphite to Si was indirectly observed through the changes in the  $\text{LiC}_x$  reflections during the relaxation period after Li metal deposition in a commercial 18650 cell. Heubner et al.<sup>42</sup> examined this effect more deeply by using an experimental set-up capable of directly recording the electrochemical interactions between the components in blended electrodes. In their experimental set-up, a graphite electrode is short-circuited with a Si electrode to mimic a blended electrode.<sup>42</sup> It was observed that during relaxation periods following charging pulses, Li is redistributed from the graphite portion of their cell to the Si portion, even at low C-rates, which is intensified at higher C-rates.<sup>42</sup> Recently, Berhaut et al.<sup>43</sup> discovered in-plane and out-of-plane concentration gradients in SiG for both the graphite and Si component. Li redistribution was observed from graphite to Si in-plane and within the different electrode sections.<sup>43</sup>

Despite these existing studies, there is still a lack of understanding on the relaxation processes in SiG anodes, especially with complimentary methods, which are validated against each other. In this study, the Li redistribution within SiG electrodes in full cells during relaxation was investigated. To gain insight into the anode charging kinetics and phase relaxation, full cells with graphite and SiG anodes of comparable cell capacity were utilized. Operando XRD and in situ microscopy measurements were compared with each other as well as results from in situ XRD measurements in relaxed cells. The process of Li redistribution is directly tracked by observing the color change of the graphite particles using the in situ optical microscopy method. In order to gain a better understanding of the lithiation state of the Si component, 3D microstructure-resolved simulations were conducted using digital twins of the full cells, as both XRD and optical microscopy only track the graphite component of the composite. The complementary analytical methods were validated against each other through the analysis of the lithiation behavior of the two cell chemistries in this multi-method approach. Finally, the results were put in context with operando diffraction studies of Li redistribution in previous studies.

## Experimental

**Materials.**—Two types of cell chemistries were examined in this study, namely graphite and Si-graphite (SiG20.8) in combination with respective NMC ( $\text{LiNi}_{0.6}\text{Mn}_{0.2}\text{Co}_{0.2}\text{O}_2$ ) cathodes. Cells with the same electrodes were previously studied by Flügel et al.<sup>44,45</sup>

The detailed description of the electrode preparation and the physicochemical properties of the anodes can be found in Ref. 44. The first cell type consisted of a graphite anode (94 wt.-% active material from Iopsilon (China), 2 wt.-% CMC binder (TIMCAL, Switzerland), 2 wt.-% SBR binder (ZEON, Japan), 2 wt.-% Super C65 (Nippon paper Industries, Japan), 3.1 mAh  $\text{cm}^{-2}$ , 1.3 g  $\text{cm}^{-3}$ , single-sided anode coating thickness: 71  $\mu\text{m}$ ) and a NMC 622 cathode (94 wt.-% active material from BASF (Germany), 2 wt.-% PVDF (Solvay, Belgium), 2 wt.-% carbon black (TIMCAL, Switzerland), 2 wt.-% graphite (TIMCAL, Switzerland), 2.63 mAh  $\text{cm}^{-2}$ , 3.2 g  $\text{cm}^{-3}$ , single-sided anode coating thickness: 50  $\mu\text{m}$ ). The electrolyte used for this cell chemistry was 1 M  $\text{LiPF}_6$  in ethylene carbonate (EC): diethylene carbonate (DEC) (3:7, wt) + 2 wt.-% vinylene carbonate (VC) (Gotion, USA).

The second cell type consisted of a Si-graphite composite (SiG) with 20.8 wt.-% of Si (Si-particles: nano-silicon embedded in a carbon matrix, 90 wt.-% active material from Iopsilon (China), 3 wt.-% CMC binder (TIMCAL, Switzerland), 3 wt.-% SBR binder

(ZEON, Japan), 4 wt.-% Super C65 (Nippon paper Industries, Japan), 3.4 mAh  $\text{cm}^{-2}$ , 1.3 g  $\text{cm}^{-3}$ , single-sided anode coating thickness: 45  $\mu\text{m}$ ) and a NMC 622 cathode (94 wt.-% active material from BASF (Germany), 2 wt.-% PVDF (Solvay, Belgium), 2 wt.-% carbon black (TIMCAL, Switzerland), 2 wt.-% graphite (TIMCAL, Switzerland), 3.30 mAh  $\text{cm}^{-2}$ , 3.2 g  $\text{cm}^{-3}$ , single-sided anode coating thickness: 66  $\mu\text{m}$ ). The electrolyte used for this cell chemistry is a 1 M  $\text{LiPF}_6$  in EC:DEC (3:7, wt) + 10 wt.-% fluoroethylene carbonate (FEC) (Gotion, USA). After formation, the N/P ratio of the graphite cell and SiG cell are 1.10 and 1.13, respectively (compare Ref. 44).

Prior to cell assembly, all electrodes were dried at 130 °C for 9 h under vacuum conditions.

**Cell manufacturing.**—Pouch cells for both cell chemistries were assembled in a dry room (dew point:  $-70$  °C) at ZSW for the XRD experiments. The cells consisted of a single-sided coated anode (26  $\text{cm}^2$ ) and a single-sided coated cathode (23.94  $\text{cm}^2$ ), and one layer of Celgard® 2325 (thickness: 25  $\mu\text{m}$ , PE/PP/PE) separator. The stack was placed in pouch bags before drying (80 °C for 16 h under vacuum conditions). Subsequently, 900  $\mu\text{l}$  of the respective electrolyte solution were added to each cell in an Ar-filled glovebox (MBraun,  $[\text{H}_2\text{O}] < 0.1$  ppm,  $[\text{O}_2] < 0.1$  ppm).

For the 3-electrode measurements, both cell chemistries were tested in PAT-EL cells with a Li-metal ring reference (EL-Cell GmbH). The separator used in these cells was a 260  $\mu\text{m}$  GF/A (Whatman plc, diameter 21.8 mm). Before assembly, the separator was dried at 230 °C under vacuum conditions overnight. Anode and cathode of equal size (2.54  $\text{cm}^2$ ; diameter: 18 mm) were used. The cells were tested at ZSW after being filled with 150  $\mu\text{l}$  of the respective electrolyte solution.

Coin half cells were manufactured at AU. There, all materials were dried in a drying oven at 80 °C under air in ambient pressure for 12 h. The CR2032 cell housing type was used for all cell tests. The cells were assembled in an Ar-filled glove box (GS Glovebox Systemtechnik GmbH;  $[\text{H}_2\text{O}] < 0.1$  ppm,  $[\text{O}_2] < 1.0$  ppm). The half cell configuration consists of the anode of full cell chemistries (diameter: 12 mm) and a Li foil counter electrode (Sigma Aldrich, 750  $\mu\text{m}$  thickness, diameter: 14 mm), with a GF/A separators (Whatman plc, diameter: 16 mm), and a Celgard® 2325 (Celgard, diameter: 16 mm) in between. The cells were filled using 150  $\mu\text{l}$  1 M  $\text{LiPF}_6$  in EC:DEC (3:7, wt) + 10 wt.-% FEC.

**Electrochemical testing.**—The formation of the full cells was conducted in a voltage window of 3.0 V–4.2 V. After 20 h under open circuit conditions, all cells were charged three times with a charge rate of 0.1 C (constant current (CC)) and were held at 4.2 V (constant voltage (CV)) until the charging current dropped to a value of 0.05 C. Discharge was performed with a discharge rate of 0.1 C. The formation of the pouch cells was performed with a BaSyTec CTS-Lab battery tester at ZSW. If not stated differently, the SOC and C-rates were referenced to the third discharge capacity of the formation.

For the in situ XRD experiments, pouch cells with different SOC were prepared. To reach the specific SOC (25%, 50%, 75%, and 100%), the cells were charged with a current of 0.1 C until the desired capacity was reached. The tests were recorded with a BaSyTec CTS-Lab battery tester at ZSW.

After formation, the PAT EL-Cells were charged one cycle with 0.1 C and one cycle with 0.5 C (CC-CV). The stop criterion for the CV step was 0.05 C. The cells were then discharged with 0.1 C and 0.5 C, respectively.

Testing of the half cells for ex situ light microscopy (LM) was conducted with a BaSyTec CTS-Lab battery tester at AU in a climate chamber (Binder) at 23 °C. The half cells were cycled between 1.5 V and 0.01 V. Charging was performed in CC-CV mode and discharging in CC mode. Lithiation was terminated when the current dropped below the 0.025 C criterion. After formation, the cells were charged in CC mode with 0.1 C and 0.5 C to 75% SOC.

**Overview on analytical methods.**—An overview of the testing parameters for the different analytical methods in this study is presented in Table I.

**Operando and in situ XRD.**—Both in situ and operando XRD experiments were recorded with a PANalytical Empyrean instrument using Mo  $K_{\alpha 1}$  ( $\lambda = 0.709 \text{ \AA}$ ) radiation with an angular range in  $2\theta$  ranging from  $6^\circ$  to  $53.5^\circ$  at MLZ. For the in situ measurement, a full pattern was recorded within 30 min, for the operando measurement, the time per pattern was 15 min. The measurements were conducted in transmission geometry using special focusing optics, so that the illumination area was  $1 \times 10.0 \text{ mm}$  in the center of the pouch cells to efficiently remove unwanted scattering from inactive cell components and to maximize the peak to background ratio. The experimental set-up is described in Ref. 46. A high efficiency GaliPIX<sup>3D</sup> detector was used to collect the diffraction pattern. The cycling of the pouch cells during operando XRD was carried out galvanostatically between 3.0 V and 4.2 V with a BioLogic potentiostat at room temperature.

For the operando measurements, the pouch cell was charged once with 0.1 C CC and held at 4.2 V CV until the charge current dropped to a value of 0.05 C. The discharge was conducted at 0.1 C. After 1 h of rest, the CC charge and discharge rates were changed to 0.5 C in the second cycle.

**Cross-sectional in situ optical microscopy.**—A detailed description of the cross-sectional in situ optical microscopy (CS-IOM) method at ZSW and the preparation of the cell can be found in Refs. 22 and 24. The gap at the edge of the in situ cell measured  $190 \mu\text{m}$  for both full cell chemistries. For assembly of the in situ optical cell, anode and cathode with the same dimensions (area  $2.1 \text{ cm}^2$ , diameter 16 mm before cutting) and two layers of 2325 Celgard separator were used (diameter: 18 mm before cutting). The cross-section was prepared by cutting with a scalpel at the sample holder edge.

The cut-off part of the electrodes were weight and the cell capacity and C-rates were calculated based on the remaining theoretical cathode capacity. Before electrolyte filling, the cells were dried for 16 h at  $80^\circ\text{C}$  under vacuum conditions. The electrolyte solution was added to the cells in two steps: the first being  $100 \mu\text{l}$ , and an additional  $50 \mu\text{l}$  being added after 1 h, inside an Ar-filled glovebox (MBraun,  $[\text{H}_2\text{O}] < 0.1 \text{ ppm}$ ,  $[\text{O}_2] < 0.1 \text{ ppm}$ ).

During operation, a custom-made digital microscope (PeciPoint) with a 40X objective was used to acquire one image every 60 s, using the stacked image mode. For the graphite cells, 150 images in a distance of  $0.25 \mu\text{m}$  were taken and merged into one image. To account for the expansion of the Si compound during (de-)lithiation, 150 images in a distance of  $0.5 \mu\text{m}$  were taken and merged into one image for the SiG20.8 cells.

The cells were charged using a Vertex.One potentiostat (Ivium Technologies B.V.). After a total soaking time of 10 h (starting from the first electrolyte filling step), the cells were charged and discharged three times with a charge rate of 0.1 C and were held at 4.2 V until the charging rate dropped to a value of 0.05 C. Then, the cells were discharged with 0.1 C.

In order to observe the relaxation of the  $\text{LiC}_x$  phases after charge, the graphite cells were charged to 3.95 V during the second cycle, while the SiG20.8 cells were charged to 3.93 V. Subsequently, images and electrochemical data of the cells were recorded for 24 h every 60 s in open circuit mode. For better visibility of the  $\text{LiC}_x$  phases, all images are adjusted by enhancing contrast and color saturation.

**Ex situ light microscopy (LM).**—To analyze the lithiation state of the half cell measurements, the cells were immediately shuttled after charging to 75% SOC into the glovebox and opened at AU. The anode was separated and rinsed with dimethyl carbonate (DMC). The time between charging termination and rinsing was about 2 min. Surface images of washed and dried anodes were captured with a ZEISS Axio Observer 7 microscope with an EC Epiplan-Neofluar 100X objective. The microscope was equipped with a neutral white (3200 K) LED and using an extended depth of field mode inside the glovebox. The images were always taken at a fixed sample position in the center of the electrode. After the first image was taken, the anodes were placed in their respective electrolyte solution for one minute for relaxation. For image acquisition, the anodes were then rinsed again with DMC and another image was taken at the same position in the electrode center. This procedure was repeated for resting periods of 5 min, 0.5 h, 1 h, 4 h, and 24 h.

**3D microstructure-resolved simulation.**—Based on particle size distributions and further characterizations of anode and cathode materials,<sup>44,47</sup> 3D digital twins were assembled in GeoDict<sup>48</sup> applying a resolution (voxel size) of  $0.438 \mu\text{m}$ . It is important to note that scanning electron microscopy images revealed that the composite anode consists barely of pure Si but rather Si nano particles in a C matrix (Si/C, compare Ref. 44). The full cell geometry was obtained by the addition of a separator ( $20 \mu\text{m}$  thickness) and current collectors.

In order to perform the simulation in the in-house software package BEST (Refs. 33, 49) at DLR, the electrolyte parameters are taken from De Lauri et al.,<sup>50</sup> the cathode parameters from Kremer et al.,<sup>51</sup> and the anode parameters are either measured, fitted, or taken from literature as summarized in Table II. Si composite material parameters are applied based on the given volume fraction. Direct exchange of Li at the interfaces of Si and graphite is neglected. Note that equilibration happens via transfer in the electrolyte. In our

**Table I. Overview of the used analytical methods in this study.**

SOC	Method	Graphite anode	SiG20.8 anode	State
0%	In situ XRD	Pouch cell	Pouch cell	Relaxed
25%	In situ XRD	Pouch Cell	Pouch Cell	Relaxed
50%	In situ XRD	Pouch Cell	Pouch Cell	Relaxed
75%	In situ XRD	Pouch Cell	Pouch Cell	Relaxed
100%	In situ XRD	Pouch Cell	Pouch Cell	Relaxed
0–100%	Operando XRD: 0.1 C	Pouch cell	Pouch cell	Not relaxed
0–100%	Operando XRD: 0.5 C	Pouch cell	Pouch cell	Not relaxed
0–100%	CS-IOM: 0.1 C	In situ optical full cell	In situ optical full cell	Not relaxed
75%	CS-IOM + 24 h relaxation	In situ optical full cell	In situ optical full cell	Not relaxed → relaxed
75%	Ex situ LM+ 24 h relaxation	Coin half cell	Coin half cell	Not relaxed → relaxed
0–100%	Simulation of 0.1 C charge	3D digital full cell	3D digital full cell	Not relaxed
25%	Simulation of 24 h relaxation	3D digital full cell	3D digital full cell	Not relaxed → relaxed
50%	Simulation of 24 h relaxation	3D digital full cell	3D digital full cell	Not relaxed → relaxed
75%	Simulation of 24 h relaxation	3D digital full cell	3D digital full cell	Not relaxed → relaxed

**Table II. Overview on measured, fitted, and literature values for the relevant parameters of the simulations.**

	Graphite	Si
Maximum concentration/mol cm <sup>-3</sup>	29,426.5 · 10 <sup>-6</sup> (calculated)	111,333.4 · 10 <sup>-6</sup> (calculated)
Open-circuit potential of active material vs Li/Li <sup>+</sup> U <sub>0</sub> /V	Measured with GITT (Fig. S1, supplementary data)	Extracted from graphite and SiG5.8 (from GITT (Fig. S1) measurements (as in Ref. 32))
Diffusion constant of Li in active material D <sub>Li</sub> /cm <sup>2</sup> s <sup>-1</sup>	3.9 · 10 <sup>-10</sup> (Ref. 52)	1 · 10 <sup>-12</sup> (Ref. 53)
Rate constant of Butler-Volmer flux k/A cm <sup>2.5</sup> mol <sup>-1.5</sup>	0.079 (Ref. 54)	Equal to graphite (assumed)
Electronic conductivity κ/S cm <sup>-1</sup>	10 (Ref. 55)	0.33 (Ref. 56)

simulations, volume changes of the Si/C composite particles are neglected, assuming that the carbon matrix acts as a buffer on particle level. For the simulation of the relaxation process, the digital twins were first charged with constant currents of 0.1 C and 0.5 C to a defined cut-off voltage corresponding to the targeted SOC (25%, 50%, and 75%). Note, that the overall transferred charge in simulation at 0.1 C and 0.5 C is therefore different due to polarization effects. The CC charging step is followed by a relaxation phase of 24 h. These simulations provide the spatial distribution of Li concentration throughout the cell for each time step of the operation, which is extracted in the results such that the bulk Li concentration corresponds to all voxels of the graphite or SiG particles, respective. The surface Li concentration corresponds to the first voxel slice towards the separator.

## Results and Discussion

**Method validation: differences in lithiation behavior during charging.**—In order to gain a better understanding on the Li redistribution behavior of the SiG composite electrodes, a graphite electrode and a SiG electrode are compared, referred to as SiG20.8, where graphite powder is mixed with 20.8 wt.-% of Si.<sup>44</sup> It is noted that the graphite compound is the same in both cases. Since graphite and Si exhibit different kinetic, electronic, and thermodynamic characteristics during lithiation,<sup>2,57,58</sup> more pronounced differences in Li redistribution with higher C-rates are expected. Therefore, C-rates of 0.1 C and 0.5 C were chosen as 0.5 C still allows for a sufficient time-resolution in the operando XRD measurements.

In 3-electrode full cells, the cell voltage and the corresponding electrode potentials were measured for the two C-rates used in this study. The results are shown in Fig. 1, indicating that compared between 0.1 C and 0.5 C charge, the graphite cells (Fig. 1a) exhibit a higher overvoltage than the SiG20.8 cells (Fig. 1c). Noticeable differences in anode potentials are observed between 0.1 C and 0.5 C for the graphite cells, while only minimal differences are present in the SiG20.8 cells. During discharge (Figs. 1b, 1d), both cell chemistries exhibit smaller overvoltage compared to the charge. In the graphite cells (Fig. 1b), the primary source of the overvoltage during discharge arises from the anode side. For discharge in the SiG20.8 cells (Fig. 1d), differences in the anode potential between 0.1 C and 0.5 C are observed between 100%–50% SOC, where the graphite component is the main contributor to the cell capacity.<sup>29,30,42,59</sup> However, there are no significant differences noticeable below 50% SOC during discharge, where Si is the main contributor.

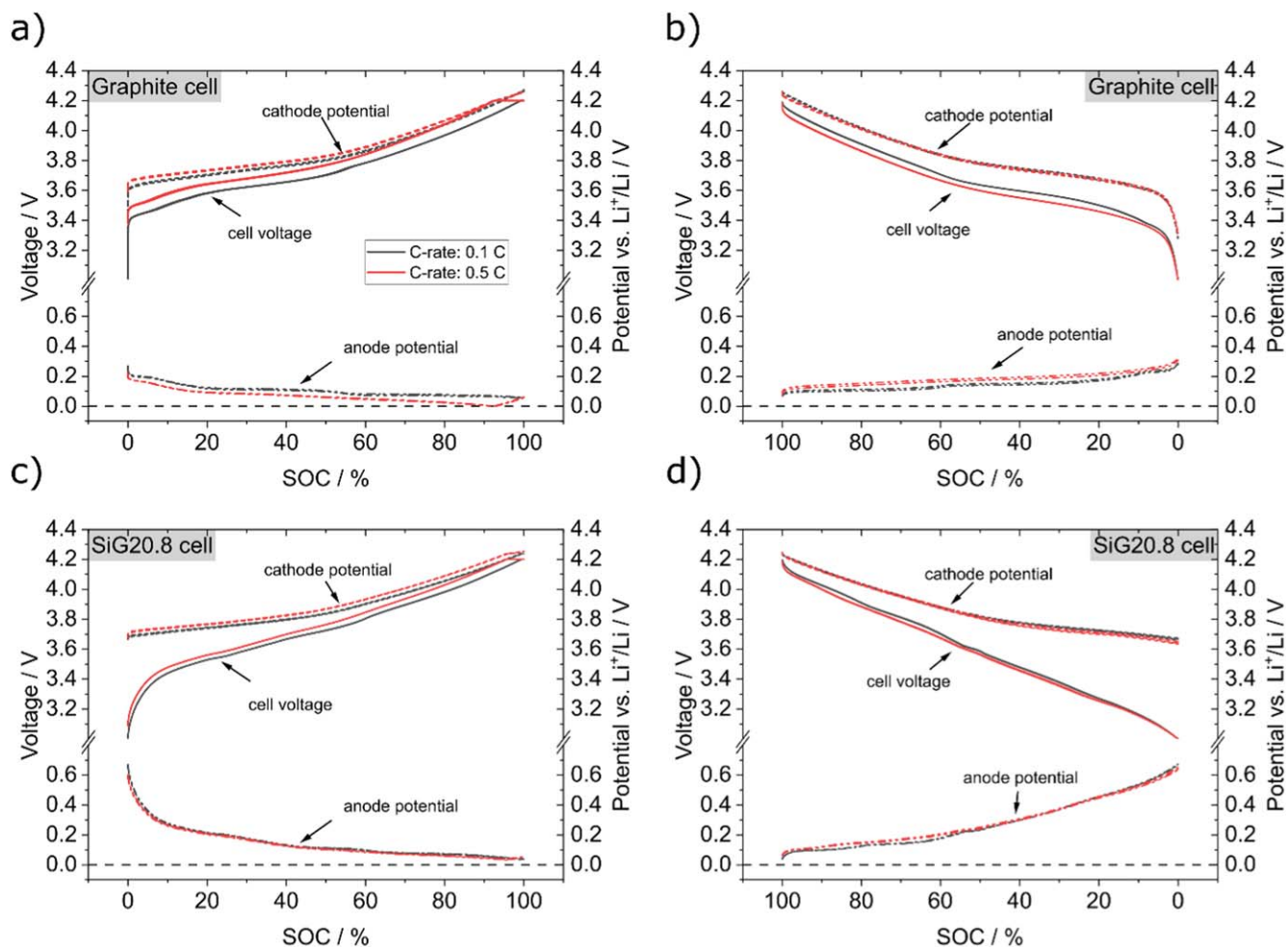
The lithiation of graphite can be tracked through operando XRD by observing the changes in the interlayer distance of the graphene sheets in the graphite crystals.<sup>16</sup> In Fig. 2, we follow the evolution of the (001) and (002) reflections of graphite and its lithiated structures in the obtained diffraction pattern during charging and discharging steps of the two C-rates. During charging, the well-known (002) Bragg reflection of graphite transforms gradually to the (002) Bragg reflection of LiC<sub>12</sub>, and finally the (001) Bragg reflection of LiC<sub>6</sub> appears at even higher lithiation states. These reflections can offer a reasonable representation of structural changes in the graphite and

SiG20.8 cells occurring during cycling. From Fig. 2a, one can observe that in the graphite cells, the (002) reflection appears at a 2θ angle of 12° at the beginning of charge, which deviates from the expected 2θ angle of delithiated graphite (12.2°, dotted line C(002)). Since the operating voltage ranges from 3.0 V to 4.2 V in this study, the graphite cell was not fully delithiated during discharge in the formation cycles. In contrast, in Fig. 2b, it is evident that the graphite component is completely delithiated in the SiG20.8 cell. The observed shifts in the (002) and (001) reflections in the SiG cell are consistent with the patterns recorded by others.<sup>28–30</sup> In the beginning of charge, the (002) reflection in the SiG20.8 cells shifts constantly, but less steeply as in the graphite cells (compare d-spacing changes in Fig. S2 in the supplementary data), which indicates that Si is being preferentially lithiated, especially until minute 200 of the measurement. After about 200 min of measurement (SOC >23%) (Fig. 2b, black arrow in Fig. S2 a in the supplementary data), the slope of the shift becomes steeper and is closer to the changes observed in the graphite cell, indicating simultaneous lithiation of the Si compound and graphite.

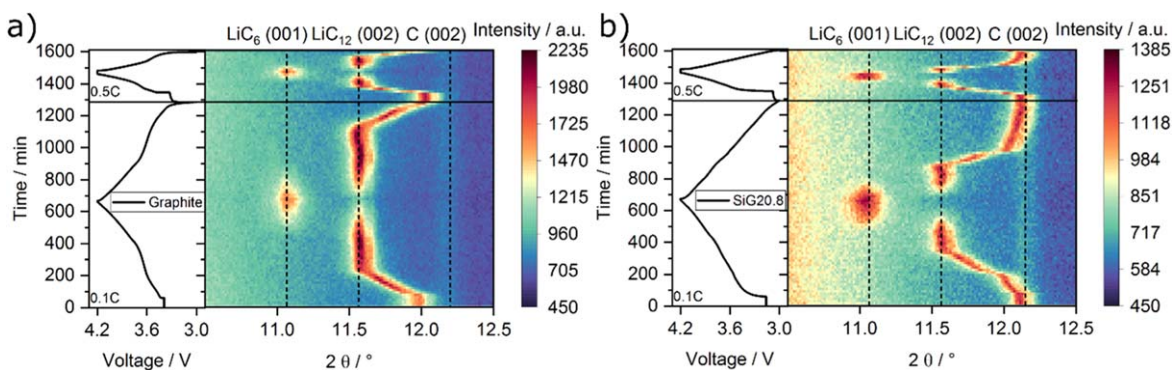
During discharge, the (002) reflection changes strongly from the 2θ angle associated with the LiC<sub>12</sub> structure to the 2θ angle associated with the C structure in the patterns from 850 min to 950 min (from 73% SOC to 55% SOC) of the operando measurement of the SiG20.8 cell. Later, only small changes are observed, indicating that mainly the Si component is active in this region. For 0.5 C data, similar asymmetric behavior of the changes in the (002) reflection is observed (compare Fig. S2b).

XRD was used to obtain information on the average lithiation state of the graphite within the bulk of the electrode. Additionally, CS-IOM was selected as a surface-sensitive method considering the expected influence of the surface concentration of the graphite particles on Li redistribution processes. The surface-sensitivity was discussed in prior measurements with the CS-IOM: In graphite-LFP full cells, the color change of the electrode occurred at the beginning of the voltage plateaus associated with the respective two-phase transitions (LiC<sub>18</sub> → LiC<sub>12</sub> and LiC<sub>12</sub> → LiC<sub>6</sub>) during a 0.1 C charge.<sup>24</sup> Furthermore, there is a color hysteresis between charging and discharging, as described in Ref. 22, suggesting that the CS-IOM a surface sensitive method, meaning only the color change of graphite particle's surfaces are observable, however not the inside of the particles.

Figure 3 compares the operando XRD patterns with CS-IOM images at selected SOC: 0%, 25%, 50%, 75%, and 100%. The corresponding cell voltages for both the operando XRD measurements and CS-IOM cells are given in Fig. 4a. Upon examining the CS-IOM images in Fig. 3b (see full video S1 for graphite and video S2 for SiG20.8 in the supplementary data), it is noticeable that the observed colors are very similar in the graphite and SiG20.8 cells at the same SOC values. This observation is unexpected considering the delayed lithiation of the graphite component in the SiG20.8 cells compared to the graphite cells. Nonetheless, when looking at the anode potentials from the 3-electrode measurements in Fig. 4b at the shown SOC of both the graphite cells and SiG20.8 cells, it becomes clear that they are similar above 50% SOC. Since the operando XRD cells, the CS-IOM cells, and the 3-electrode EL-cells all display



**Figure 1.** Cell voltage and corresponding anode and cathode potentials in 3-electrode full cells at 0.1 C (black lines) and 0.5 C (red lines) during charge of for the graphite cells (a) and SiG20.8 cells (c) and during discharge (b) and (d), respectively. The dashed line highlights 0 V vs  $\text{Li}^+/\text{Li}$ . The SOC was normalized to the end-of-charge or end-of-discharge capacity, respectively.



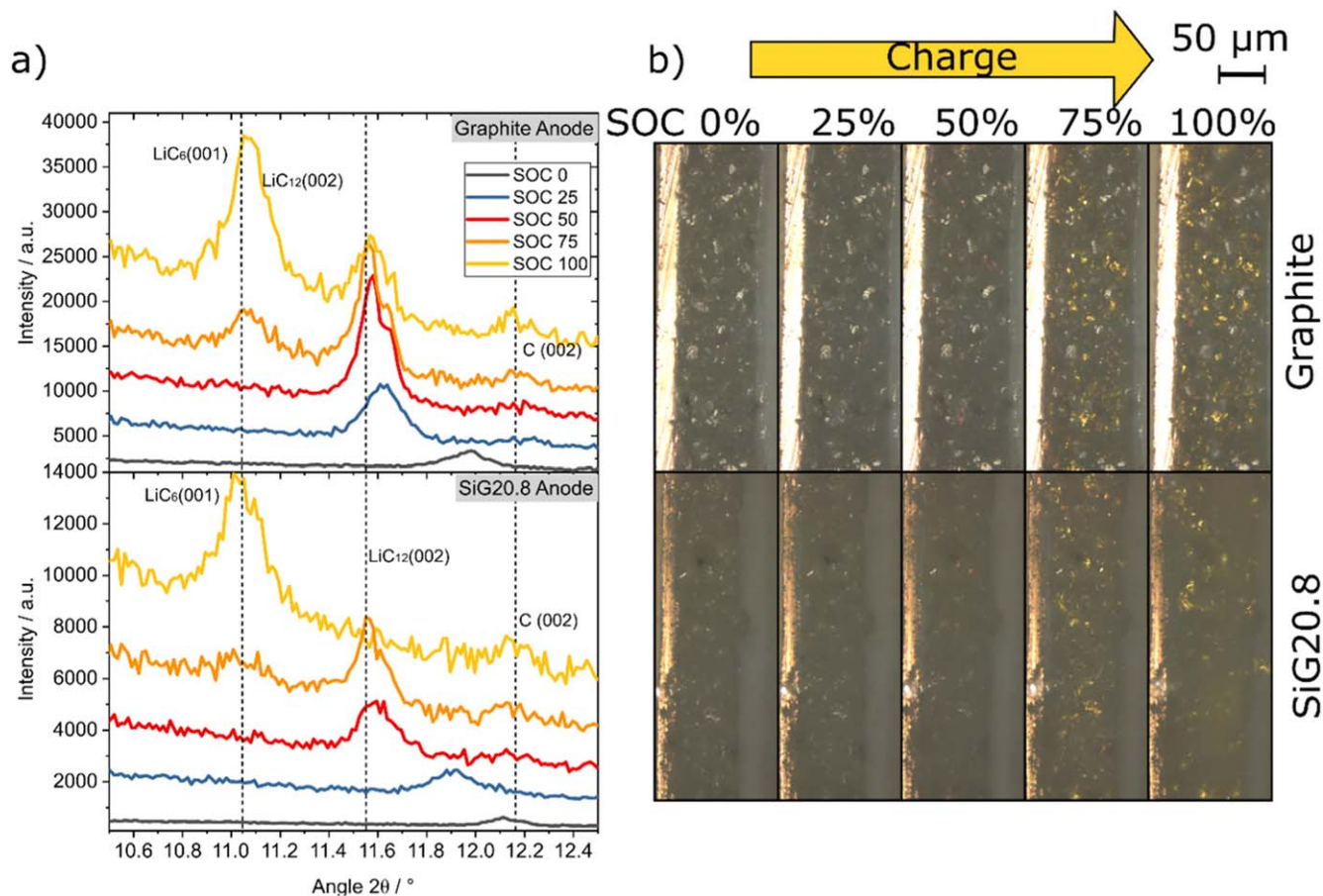
**Figure 2.** (a) Contour plot representation of the operando XRD measurements for the graphite pouch full cell at 0.1 C and 0.5 C. The corresponding galvanostatic cycles are shown in the left panel. The  $2\theta$  positions of the (002) Bragg reflections of the C and  $\text{LiC}_{12}$  structures as well as the (001) Bragg reflection of  $\text{LiC}_6$  structure are highlighted by vertical dotted lines. (b) Contour plot representation of the operando XRD measurements for the SiG20.8 pouch full cell.

comparable cell voltage curves (Fig. 4), we assume that the anode potential for all cell types are comparable at 0.1 C. This explains why no significant difference can be observed above 50% SOC, where the microscopy method is most sensitive to the color change Fig. 3b.

In the XRD measurements (Fig. 3a), more distinct differences in the lithiation state between graphite and SiG20.8 are observable, particularly at low SOC (0% and 25%), which also fits the anode potential differences (Fig. 4b). At higher lithiation states (SOC:

50%, 75%, and 100%), both cell chemistries demonstrate the same reflections ( $\text{LiC}_{12}$  at 50% SOC, both  $\text{LiC}_{12}$  and  $\text{LiC}_6$  for 75% and 100%) with different intensities. The reflections of  $\text{LiC}_6$  were recorded in both graphite and SiG20.8 full cells at 75% and 100% SOC, which is consistent to the golden color of the electrode in the CS-IOM measurement (Fig. 3b).

When examining the calculated Li content in the graphite component during the 0.1 C charge at 75% SOC (Table S3), it is noticeable that the Li content in graphite is very similar under these



**Figure 3.** (a) 1D XRD patterns from the operando XRD measurement in Fig. 2 at selected SOC values: 0% (grey), 25% (blue), 50% (red), 75% (orange), and 100% (yellow) for both graphite (upper panel) and SiG20.8 (lower panel) full cells for the 0.1 C charge. The vertical dotted lines highlight the  $2\theta$  positions of the (002) reflection of the C and  $\text{LiC}_{12}$  structures as well as the (001) reflection of the  $\text{LiC}_6$  structure. The pattern is shifted in y-direction for better visibility. (b) Corresponding images of the graphite (video S1 in supplementary data) and SiG20.8 (video S2 in supplementary data) anodes from the CS-IOM measurement at the same SOC values as in (a).

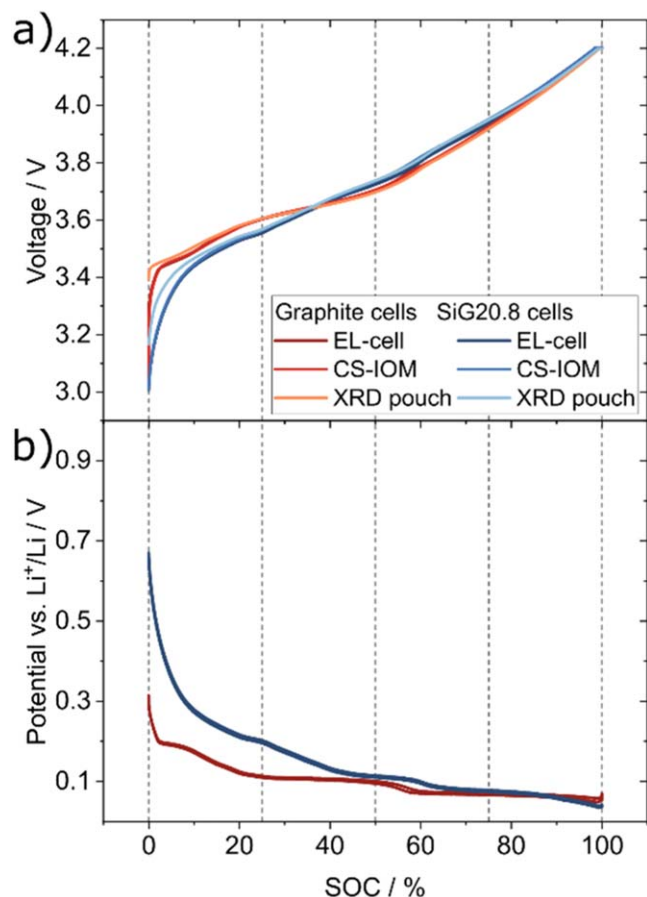
conditions. However, comparing the operando XRD measurements to the in situ XRD measurements, a slightly increased Li content in the graphite component of 0.04–0.06 is noticeable in the operando measurements. This indicates internal Li redistribution between graphite and Si, which will be discussed in the subsequent section. It has to be noted that Li content from XRD in graphite in both graphite cell and SiG cell is only a rough estimation due to the low intensity and low signal-to-noise ratio of the in situ and operando measurements. Additionally, it is noticeable for the 0.5 C charge that the Li content in the graphite component in the SiG20.8 cell is considerably higher than during the 0.1 C charge, indicating a preferred lithiation of graphite at higher C-rates. We can attribute this effect to kinetic limitations of Li in the Si material. This is illustrated in simulated concentration distributions presented in Fig. S4.

The experimental findings are supported by the results of the normalized Li concentrations obtained in the simulations as depicted in Fig. 5. Figure 5a shows the average normalized Li concentration in the bulk of the anode as well as the maximum at the anode surface near the separator in the digital twins for both the graphite (Fig. 5b) and the SiG20.8 cell (Fig. 5c) during the 0.1 C charge simulation.

While on the one hand the operando XRD data and the bulk concentration in the graphite matches up, on the other hand, the CS-IOM and the surface concentration also fit together. It is important to note that our measurements were conducted in full cells and therefore, 100% SOC does not correspond to a fully lithiated anode, which is represented by the normalized Li concentration of 0.8 at 100% SOC in the graphite full cell.

As expected, a linear increase in the average Li concentration is observed in the graphite cell (black solid line in Fig. 5a). At the graphite electrode surface, a higher Li concentration than the average value was observed. This is due to lithiation gradients arising from transport limitations in the electrolyte. This observation is consistent with previous CS-IOM observations with different cell chemistry.<sup>22,24</sup>

In case of the SiG20.8 cell, a delayed lithiation of the graphite component in SiG20.8 is evident. At the beginning of the charging process (SOC < 75%) the average normalized Li concentration of graphite in the composite electrode (cyan solid line in Fig. 5a) is well below the normalized Li concentration in the electrode consisting of graphite only. This observation is similar to the results from operando XRD measurements (Fig. 3). In contrast, the average normalized Li concentration in Si of the composite electrode increases rapidly at the beginning of the charging process (Fig. 5a, dark blue solid line). However, above 50% SOC we observe preferential lithiation of graphite in the composite, where the slope of the normalized concentration over SOC is an indicator for lithiation rates. Lithiation of the materials is mainly driven by the open-circuit potentials (OCP) of graphite and Si (see Fig. S1). Due to the higher OCP of Si compared to graphite for normalized Li concentrations smaller than 80%, Si is lithiated preferentially at the beginning. At 50% SOC the lithiation fraction at the surface of Si particles, represented by the lithiation fraction close to the separator, reaches 80%. Eventually, the graphite OCP is higher than that of Si favoring the rapid lithiation of graphite. Above 80% SOC the normalized concentration in Si is higher than in graphite for the



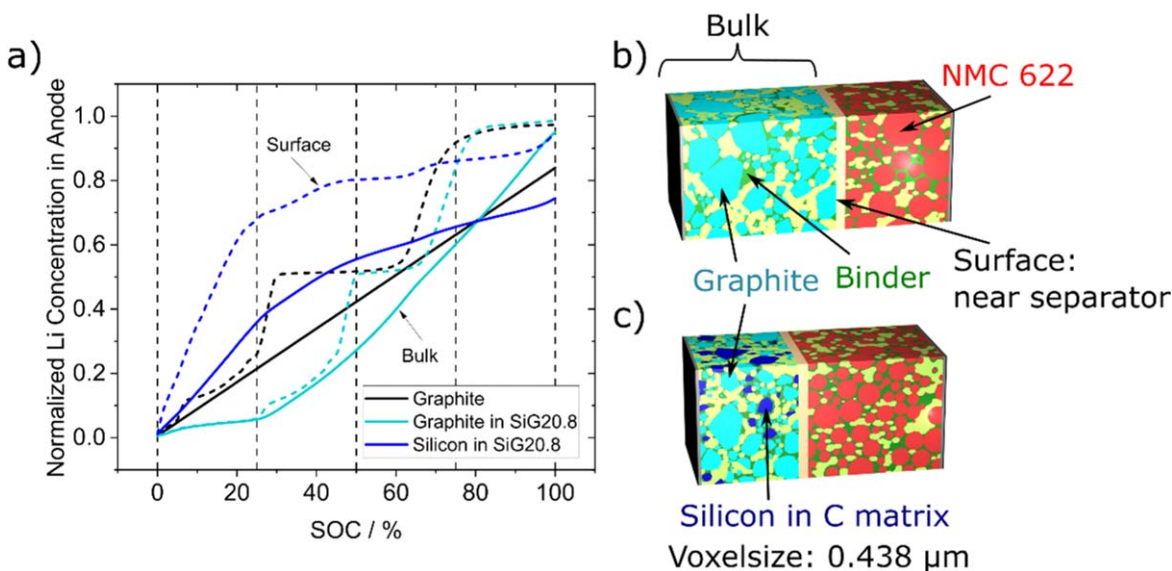
**Figure 4.** (a) Comparison of cell voltage of the graphite cell (red/orange lines) and SiG20.8 cell (blue lines) in the different cell formats (dark red/dark blue: EL-Cell; medium red/blue: CS-IOM; orange/light blue: operando XRD pouch cell) at 0.1 C. The vertical dashed lines highlight the SOC values shown in Fig. 3(b) Anode potential from the 3-electrode cells.

composite materials. Qualitative trends are consistent with previous reports.<sup>31,34,42</sup>

At 100% SOC, the lithiation state of the graphite component is higher than in the Si component (compare cyan and dark blue solid lines at 100% SOC in Fig. 5a). The  $\text{LiC}_x$  reflections measured with XRD are in good agreement with the simulation outcome when comparing them to the normalized Li concentrations of the bulk at 25%, 50%, 75%, and 100% SOC. However, only at 0% SOC significant deviations between the experimental and simulation results are observable. The simulation does not consider the residual Li in the graphite electrode after formation for the graphite cells (cell voltage from simulation in Fig. S3 in the supplementary data). Overall, the observations emphasize the agreement of the methods. Note, that the surface dynamics of Li insertion (dashed lines in Fig. 5a) are qualitatively similar. In the composite electrode, graphite is the first material to reach high local concentrations. This indicates a risk of Li depositions on the graphite particles of SiG electrodes at high SOCs.

In the in situ optical measurements, distinction of the colors blue ( $\text{LiC}_{18}$ )<sup>19,20</sup> and red ( $\text{LiC}_{12}$ )<sup>19,20</sup> is very difficult and no real differences between the graphite cells and SiG20.8 cells can be observed in the images (Fig. 3b). However, the simulations in Fig. 5a reveal a lower lithiation degree in graphite. At 50% and 75% SOC, the normalized Li concentration at the surface is comparable for the graphite cell and the graphite component in the SiG20.8 (Fig. 5a, black and cyan dashed lines). Such small differences in normalized Li concentration (50%: 0.5 both; 75%: 0.8 or 0.9) cannot be differentiated with the CS-IOM, as the graphite electrodes in the CS-IOM cells appeared golden at SOC values higher than 70% in previous publications.<sup>22,24</sup> Therefore, the results obtained by the simulations in Fig. 5a support the CS-IOM observations in Fig. 3b.

Overall, our findings demonstrate the agreement and the complementary aspects of the utilized methods. XRD effectively tracks the average lithiation degree in the graphite component, while the CS-IOM is better suited to examine the phases formed at the surface of the graphite particles. Moreover, 3-electrode measurements and 3D microstructure-resolved simulations validate the observed lithiation states in both XRD and CS-IOM. Furthermore, the simulations allow for the deduction of the Li concentration in Si, which cannot be directly measured by the other two methods. With this, not only



**Figure 5.** (a) SOC dependent normalized Li concentration in graphite in the graphite cell (black), and graphite (cyan), and Si (blue) in the SiG20.8 cell from 3D resolved microstructural simulations of 0.1 C charge. The dashed line gives the concentration at the electrode surface near the separator, the solid line the averaged value of the electrode bulk. The vertical dashed lines emphasize the SOC values from Fig. 3. (b) Digital twin of the graphite cell and (c) the SiG20.8 cell. The blue particles represent Si (70%) in a carbon matrix (30%). The separator is not in scale for improved visualization.



are the methods validated, but a foundation for an even more precise analysis of the Li dynamics is established. Thus, these methods are utilized for studying the Li redistribution processes after charging in detail in the next section.

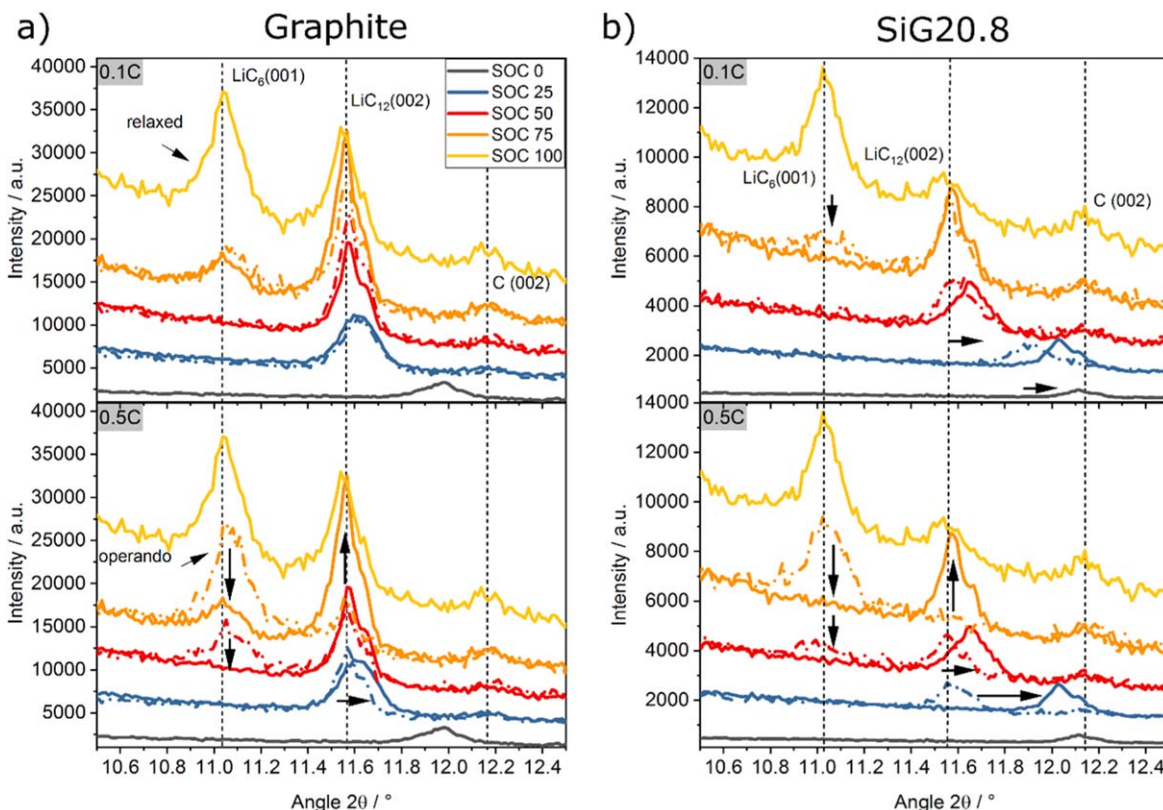
**Li redistribution processes after charging.**—Significant differences in the lithiation degree of graphite and Si in SiG20.8 during the charging process suggest the occurrence of Li redistribution if the cells are allowed to relax at different SOC. For further investigation, in situ XRD measurements in pouch cells at different SOC were performed. The results are presented in Fig. 6, including the patterns of the same SOC values from the operando measurements. As expected, the graphite cells exhibit no significant differences between relaxed cells (solid lines in Fig. 6a) and those during operation at 0.1 C (dash-dotted lines in Fig. 6a). At 0.5 C, differences in the intensities at 50% SOC and 75% SOC for the reflections associated with  $\text{LiC}_{12}$  and  $\text{LiC}_6$  are noticeable, indicating equilibration within the graphite electrodes due to lithiation gradients.<sup>60–62</sup>

For the SiG20.8 cells, shifts in the Bragg reflections are already observed at 0.1 C (Fig. 6b). A shift of the (002) reflection towards lower lithiation degrees compared to the operando measurement is observed in the relaxed cells at 25%, 50%, and 75% SOC. This phenomenon is even more pronounced at 0.5 C. For instance, the  $\text{LiC}_6$  phase is already detected at 50% SOC in the operando cell, which is similar to the graphite cell. This indicates that at higher C-rates graphite lithiation becomes more favorable, which is consistent with findings in model blended SiG electrodes.<sup>42</sup> In the relaxed state, the  $2\theta$  position of the (002) reflection is not at the  $\text{LiC}_{12}$  position anymore but shifted towards lower lithiation degrees. Presumably, both the equilibration due to lithiation gradients between graphite particles and the redistribution of Li from graphite into Si occur during the relaxation after charging at 0.5 C.

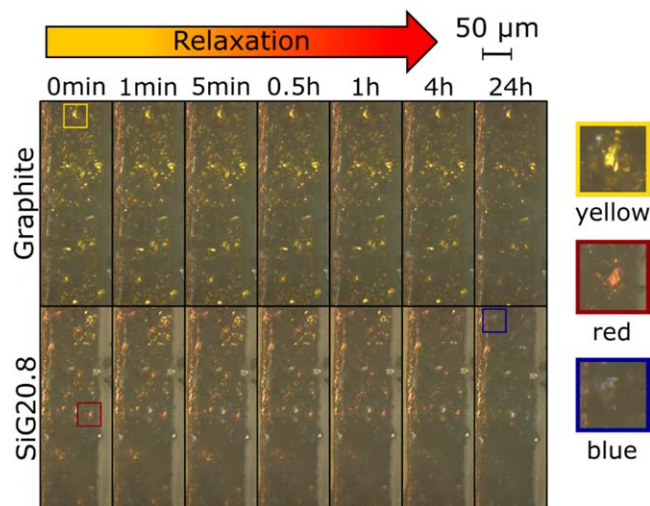
To directly observe the redistribution of Li, the CS-IOM cells were charged to 75% SOC with 0.1 C, followed by a 24 h relaxation period (compare supplementary data video S3). The SOC of 75% was chosen, since the optical measurements are most sensitive to the color change at the corresponding lithiation degree, as discussed in the previous section.

The graphite cell images (Fig. 7, upper panel) display a subtle color change from yellow to red, indicating equalization of charge within the particles. During relaxation in the SiG 20.8 cell (Fig. 7, lower panel), the color change is more pronounced. At the beginning of the relaxation (0 min), both red ( $\text{LiC}_{12}$ ) and gold ( $\text{LiC}_6$ ) are observable. However, the golden color disappears within the first 4 h. For instance, comparing the color of the graphite particle with the blue border for SiG20.8 at 24 h ( $\text{LiC}_{18}$ ) and the particle during 0 min–1 h at the same position (Fig. 7, lower panel) shows that this particle was golden ( $\text{LiC}_6$ ) before. By the end of the relaxation, the electrode appears predominantly blueish-grey, indicating a lithiation degree below  $\text{LiC}_{12}$ . This observation is consistent with the XRD measurements and suggests a redistribution of Li from graphite to Si.

Due to the reduced resolution of the CS-IOM images, especially in the SiG20.8 cells, ex situ LM was conducted to confirm the observed colors in Fig. 7. The results of the top view images are shown in Fig. 8. At 0.1 C (Fig. 8a), no color changes during the relaxation period are observable in the graphite cells. For the SiG20.8 cells, most of the visible  $\text{LiC}_6$  disappears within the first 4 h of relaxation similar to the in situ CS-IOM measurement. The color of the electrode appears blue and red after 24 h relaxation. A preferred lithiation of graphite is evident by the more apparent presence of  $\text{LiC}_6$  on the electrode surface after the 0.5 C charge. Again, the majority of color changes occur during the first 4 h of the relaxation. Furthermore, the Li redistribution appears to be more pronounced in the SiG20.8 electrode after 0.5 C charging (Fig. 8b), which corresponds to the observations from the XRD measurements (Fig. 6).



**Figure 6.** Operando (dash-dotted lines) and in situ (solid lines) 1D XRD patterns at selected SOC: 0% (grey), 25% (blue), 50% (red), 75% (orange), and 100% (yellow) for the graphite full cell (a) and SiG20.8 full cell (b) at 0.1 C (upper panel) and 0.5 C (lower panel). The patterns are shifted in y-direction for better visibility. The in situ 1D XRD pattern is from the relaxed cells in all cases. The bold arrows indicate the signal shift during relaxation.



**Figure 7.** Selected images from the image sequence during the relaxation time (0–24 h) from the CS-IOM measurements in full cells for the graphite anode (upper panel) and SiG20.8 anode (lower panel, video S3) cell, after being charged to 75% SOC with 0.1 C. The insets on the right-hand side are magnifications of the particles with the same border color in the image sequences.

Finally, the results gained from relaxation simulations after charge are considered. Figure 9 shows the normalized Li concentration in graphite and Si during the relaxation period after charging to different SOC values (25%, 50%, and 75%) with 0.1 C and 0.5 C. In all cases, the most significant changes are noticeable in the initial few hours of relaxation.

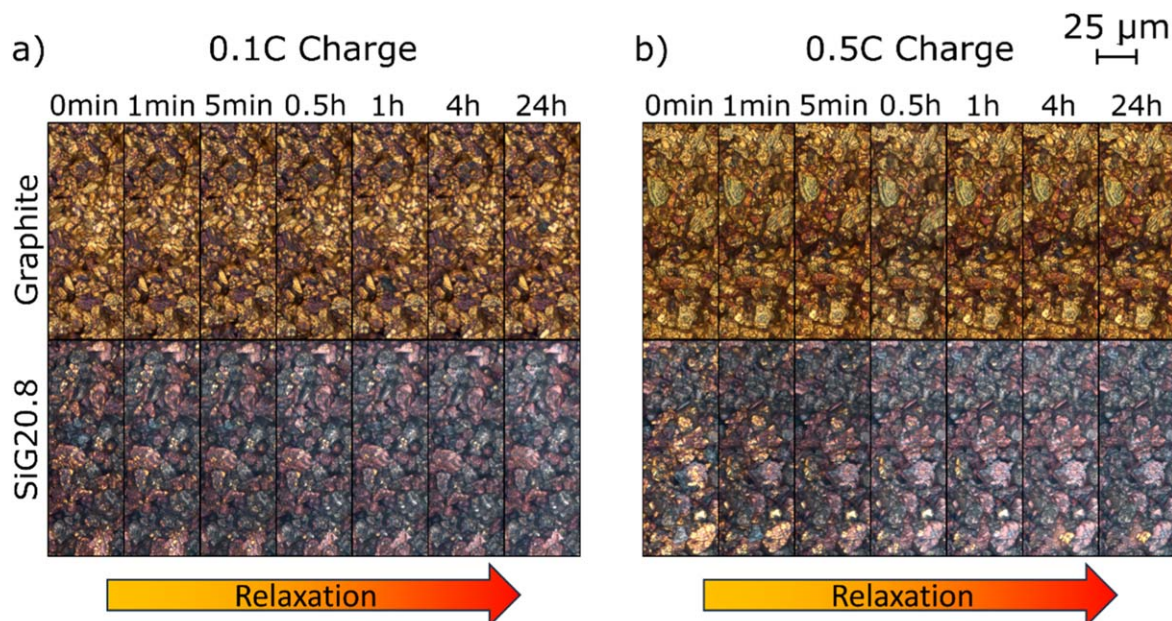
Li was redistributed from graphite to Si in the SiG20.8 cell as shown by the change in the respective bulk concentrations. This is in line with the XRD and microscopy measurements. Even at a low C-rate of 0.1 C (Figs. 9a, 9c, 9e), the average Li concentration in graphite particles decreases during relaxation, while the Li concentration in Si increases. This trend is even more pronounced at 0.5 C (Figs. 9b, 9d, 9f). At 75% SOC (Fig. 9f), the normalized Li concentration in the graphite compound is even higher than in Si, in contrast to the other cases. These results show that the lithiation of graphite is kinetically favored compared to Si with higher C-rate as

higher normalized concentrations are reached at the end of CC charging (see Fig. S1). This aligns with the observations of the operando XRD measurements (Fig. 6a), where graphite exhibits higher degrees of lithiation at 25%, 50%, and 75% SOC during the 0.5 C charge, in contrast to the 0.1 C charge. Qualitative agreement of simulations and operando measurements indicates that effective Li dynamics of the Si material in our study are indeed slower compared to graphite (Fig. 9, Table II).

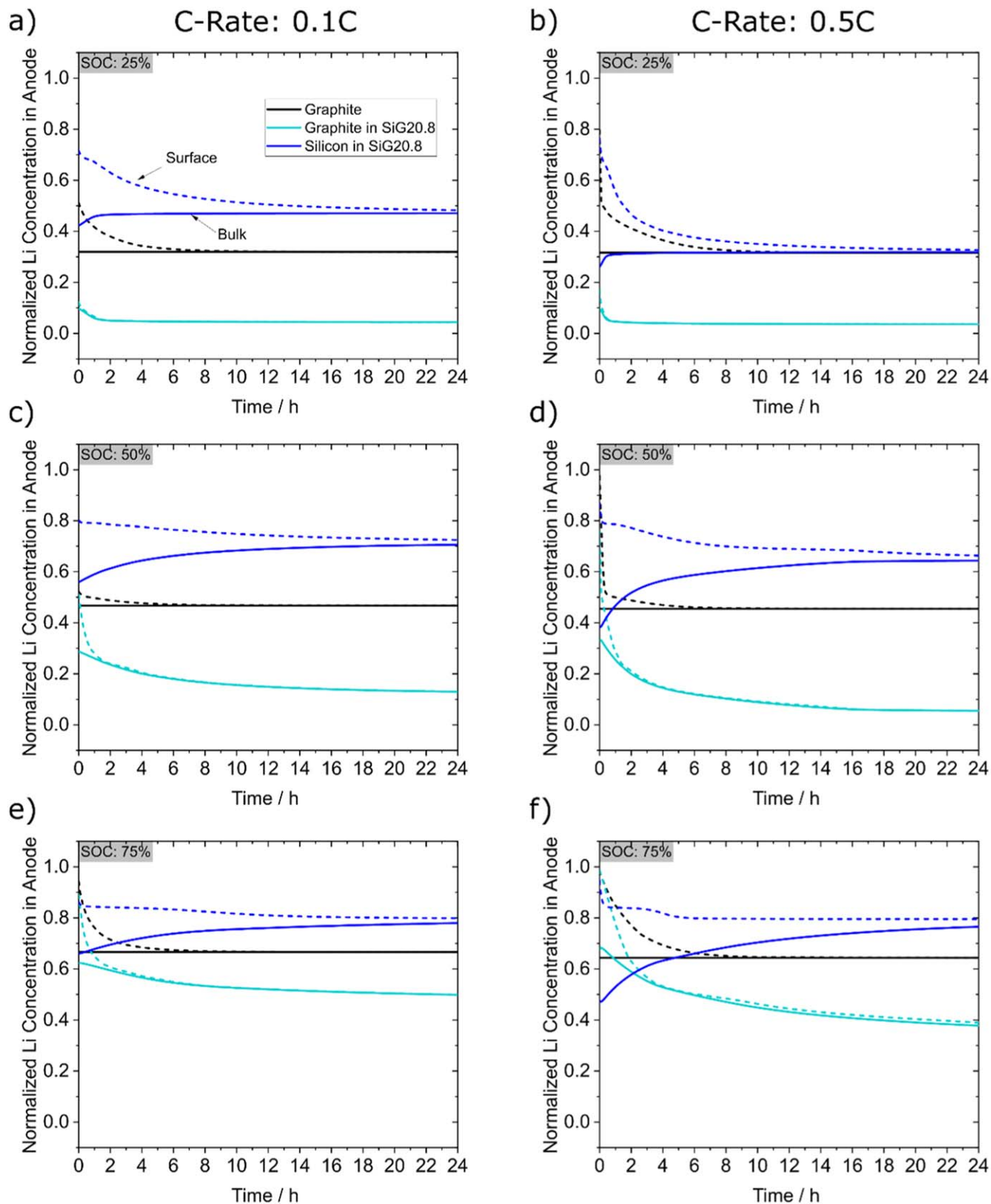
As expected, the surface concentration is higher than the average value and exhibits a significant decline throughout the relaxation period (dotted lines in Fig. 9). Since a similar phenomenon is observed in the pure graphite cell as well, it confirms the simultaneous occurrence of two relaxation processes within the SiG20.8 electrode by our simulations: (1) Equilibration throughout the electrode due to local differences in the lithiation state, as previously reported by others,<sup>43,62</sup> and (2) equilibration between graphite and Si particles, as previously observed in experiments conducted by others.<sup>39,41–43</sup>

Figure 10 provides a summary of the observed Li redistribution processes within SiG composite electrodes. Even after charging at a low C-rate of 0.1 C, Li is moving from graphite to Si at the selected SOC values (25%, 50%, 75%). At 0.5 C, an additional equilibration process is assumed between particles close to the surface and those closer to the current collector, as it was observed in the pure graphite electrodes and by Berhaut et al.<sup>43</sup> in SiG electrodes. Richter et al.<sup>41</sup> reported a similar redistribution of Li from graphite to the Si compound in a commercial 18650 cell during low temperature operando neutron-scattering measurements following Li metal deposition and re-intercalation. After Li metal deposition, the authors initially observed an increase in the lithiation degree in the graphite component due to the intercalation of the deposited Li metal into the graphite,<sup>41</sup> as it was also previously reported for pure graphite electrodes.<sup>60,61</sup> Nevertheless, during the second part of the relaxation period, a decrease in the lithiation degree of the graphite component was observed,<sup>41</sup> consistent to the operando XRD measurements in the present study. Richter et al. interpreted their results as a redistribution of Li from graphite to Si.<sup>41</sup> Our findings in lab-scale pouch cell experiments on Li redistribution confirm their results<sup>41</sup> as well as the experiments by Heubner et al.<sup>42</sup> on model blended SiG electrodes, who observed similar Li redistribution after pulse charging.

In everyday battery use, such as home storage, portable devices, or battery electric vehicles, batteries are seldomly charged from SOC



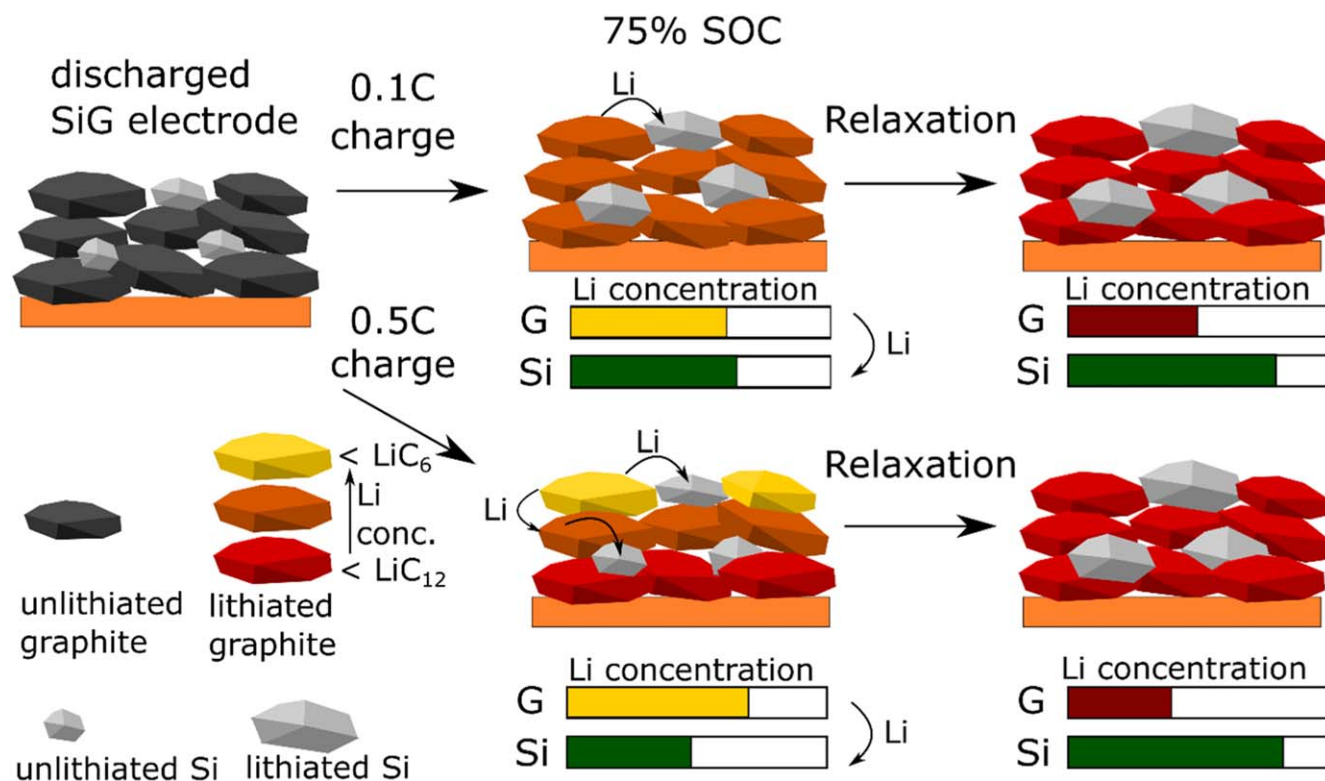
**Figure 8.** Ex situ LM images of the graphite and SiG20.8 electrode after charging to 75% SOC with 0.1 C (a) and 0.5 C (b) in half cells.



**Figure 9.** Normalized Li concentration from the 3D microstructure-resolved simulations in the anode bulk (solid lines) and at the surface (dotted lines) for graphite in the graphite cell (black) and graphite (cyan) and Si (blue) in the SiG20.8 cell during the 24 h relaxation period after being charged (a) to 25% SOC with 0.1 C, (b) to 25% SOC with 0.5 C, (c) to 50% SOC with 0.1 C, (d) to 50% with 0.5 C, (e) to 75% SOC with 0.1 C, and (f) to 75% SOC with 0.5 C.

0% to SOC 100%. Instead, they are more likely charged to SOC values in between. Consequently, Li redistribution processes in blended or composite electrodes are a real event and might affect the

aging of the different active materials and therefore also the battery. In previous studies, one reported source of aging in Si electrodes was Li trapping in the core of Si particles.<sup>11,63</sup> Delithiated Si has a lower



**Figure 10.** Sketch of the Li redistribution processes observed during relaxation in this study after charging to 75% SOC with 0.1 C and 0.5 C.

Li diffusivity compared to lithiated Si.<sup>11</sup> As a result, Li becomes trapped inside the core of the Si particle during discharge, creating lithiation gradients within the material.<sup>11</sup> Therefore, Li redistribution from graphite to Si might lead to Li trapping in the subsequent discharge. Further research is required to draw conclusions on this subject. Overall, the understanding of internal Li redistribution processes can be beneficial for a better understanding of material aging and optimization of electrode design for LIBs.

### Conclusions

The charge and redistribution mechanisms of Li within SiG electrodes were analyzed in full cells by using bulk sensitive methods (in situ and operando XRD), surface sensitive methods (ex situ and in situ optical (light) microscopy), and 3D microstructure-resolved simulations. The methods were successfully validated against each other through the comparison of the Li distribution during charging, building the foundation for an even more precise characterization.

The simulations allowed the analysis of the Li content in Si particles within the composite electrode, as both XRD and optical microscopy are not able to monitor the lithiation state in the Si component. Our study connects these complementary analysis methods and enables their validation by comparison of their results. All methods yielded consistent results, showing the simultaneous lithiation of the graphite and Si components in the SiG electrodes during charging.

The analysis of relaxed cells and cells during operation, in combination with direct monitoring of the relaxation period, provided insights into the Li redistribution after charging of full cells with anodes containing 20.8 wt.-% Si to 25%, 50%, and 75% SOC with 0.1 C and 0.5 C. The changes of the intensity and  $2\theta$  position of the (001) and (002) Bragg reflections of the graphite compound in the SiG20.8 cells in operando XRD and in situ XRD of the relaxed cells at the respective SOC values showed a shift towards a lower lithiation degree, suggesting Li is distributed from graphite

to Si. During in situ optical microscopy and ex situ LM measurements, the disappearance of the yellow  $\text{LiC}_6$  within 24 h after charging was directly observed in the SiG20.8 cells at both C-rates, whereas the graphite cells exhibited no significant color change during the 24 h relaxation period. In the simulation, the reduction of the Li content in the graphite component could be seen, while the Li content in Si increased simultaneously.







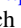



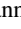
The redistribution of Li from graphite to Si was found at SOC 25%, 50%, and 75% SOC for all applied analytical methods, even after 0.1 C charging. This effect was more pronounced at 0.5 C. An overview on the proposed redistribution processes is shown in Fig. 10. The graphite component exhibited a higher lithiation state in the SiG20.8 cells at the analyzed SOC values at 0.5 C (operando XRD, ex situ LM, simulation), implying a favored lithiation of graphite over Si at higher C-rates. Potential impact of Li redistribution processes on battery aging are briefly discussed, as they might favor Li trapping inside the Si component.

Our study shows the clear advantage of combining complementary advanced experimental methods and simulations. For further understanding, the development and application of new methods which are sensitive to the Li concentration in Si are required.

### Acknowledgments

The authors from ZSW, DLR, AU, and TUM would like to acknowledge the German Federal Ministry of Education and Research (BMBF) for funding and support of the project CharLiSiKo (03XP0333) in the AQua-Cluster under the project management by Projektkrager Julich (PTJ). XRD measurements have been performed at the Physics Lab of Heinz Maier-Leibnitz Zentrum at TUM. The work performed at DLR contributes to the research at CELEST (Center for Electrochemical Energy Storage Ulm-Karlsruhe). The simulations were carried out at JUSTUS 2 cluster supported by the state of Baden-Wurttemberg through bwHPC and the German Research Foundation (DFG) through grant No INST 40/575-1 FUGG.

## ORCID

Christin Hogrefe  <https://orcid.org/0000-0001-9952-8507>  
 Neelima Paul  <https://orcid.org/0000-0002-6906-1683>  
 Lioba Boveleth  <https://orcid.org/0000-0001-9283-2397>  
 Marius Bolsinger  <https://orcid.org/0009-0008-9818-1095>  
 Marius Flügel  <https://orcid.org/0000-0002-9792-0414>  
 Timo Danner  <https://orcid.org/0000-0003-2336-6059>  
 Arnulf Latz  <https://orcid.org/0000-0003-1449-8172>  
 Ralph Gilles  <https://orcid.org/0000-0003-2703-4369>  
 Volker Knoblauch  <https://orcid.org/0000-0001-9075-9085>  
 Margret Wohlfahrt-Mehrens  <https://orcid.org/0000-0002-5118-5215>  
 Markus Hölzle  <https://orcid.org/0009-0004-8278-1089>  
 Thomas Waldmann  <https://orcid.org/0000-0003-3761-1668>

## References

- F. Luo, B. Liu, J. Zheng, G. Chu, K. Zhong, H. Li, X. Huang, and L. Chen, *J. Electrochem. Soc.*, **162**, A2509 (2015).
- M. N. Obrovac and L. Christensen, *J. Power Sources*, **7**, A93 (2004).
- J. Li and J. R. Dahn, *Solid State Ionics*, **154**, A156 (2007).
- J. P. Maranchi, A. F. Hepp, and P. N. Kumta, *J. Electrochem. Soc.*, **6**, A198 (2003).
- M. N. Obrovac and L. J. Krause, *J. Power Sources*, **154**, A103 (2007).
- C. Zhang, F. Wang, J. Han, S. Bai, J. Tan, J. Liu, and F. Li, *Small Structures*, **2**, 2624 (2021).
- E. Pollak, G. Salitra, V. Baranchugov, and D. Aurbach, *J. Phys. Chem. C*, **111**, 11437 (2007).
- J. Pan, Q. Zhang, J. Li, M. J. Beck, X. Xiao, and Y.-T. Cheng, *Nano Energy*, **13**, 192 (2015).
- J. Li, X. Xiao, F. Yang, M. W. Verbrugge, and Y.-T. Cheng, *J. Phys. Chem. C*, **116**, 1472 (2012).
- J. Xie, N. Imanishi, T. Zhang, A. Hirano, Y. Takeda, and O. Yamamoto, *Mater. Chem. Phys.*, **120**, 421 (2010).
- L. S. de Vasconcelos, R. Xu, and K. Zhao, *J. Mech. Phys. Solids*, **144**, 104102 (2020).
- M. S. Dresselhaus and G. Dresselhaus, *Adv. Phys.*, **51**, 1 (2002).
- M. Kim, D. C. Robertson, D. W. Dees, K. P. Yao, W. Lu, S. E. Trask, J. T. Kirner, and I. Bloom, *J. Electrochem. Soc.*, **168**, 70506 (2021).
- H. Yang, H. J. Bang, and J. Prakash, *J. Electrochem. Soc.*, **151**, A1247 (2004).
- P. Li, H. Kim, S.-T. Myung, and Y.-K. Sun, *Energy Storage Mater.*, **35**, 550 (2021).
- J. R. Dahn, *Physical Review B, Condensed Matter*, **44**, 9170 (1991).
- S. Schweidler, L. de Biasi, A. Schiele, P. Hartmann, T. Brezesinski, and J. Janek, *J. Phys. Chem. C*, **122**, 8829 (2018).
- K. P.-C. Yao, J. S. Okasinski, K. Kalaga, I. A. Shkrob, and D. P. Abraham, *Energy Environ. Sci.*, **12**, 656 (2019).
- R. Juza and V. Wehle, *Naturwissenschaften*, **52**, 560 (1965).
- K. C. Woo, W. A. Kamitakahara, D. P. DiVincenzo, D. S. Robinson, H. Mertwoy, J. W. Milliken, and J. E. Fischer, *Phys. Rev. Lett.*, **50**, 182 (1983).
- S. J. Harris, A. Timmons, D. R. Baker, and C. Monroe, *Chem. Phys. Lett.*, **485**, 265 (2010).
- C. Hogrefe, T. Waldmann, M. B. Molinero, L. Wildner, P. Axmann, and M. Wohlfahrt-Mehrens, *J. Electrochem. Soc.*, **169**, 50519 (2022).
- S. Kang, S. J. Yeom, and H.-W. Lee, *ChemSusChem*, **13**, 1480 (2020).
- C. Hogrefe, T. Waldmann, M. Hölzle, and M. Wohlfahrt-Mehrens, *J. Power Sources*, **556**, 232391 (2023).
- Y. Qi and S. J. Harris, *J. Electrochem. Soc.*, **157**, A741 (2010).
- M. K. Cho, S. J. You, J. G. Woo, J.-C. An, S. Kang, H.-W. Lee, J. H. Kim, C.-M. Yang, and Y. J. Kim, *Composites Part B: Engineering*, **215**, 108799 (2021).
- D.-H. Yoon, M. Marinaro, P. Axmann, and M. Wohlfahrt-Mehrens, *J. Electrochem. Soc.*, **167**, 160537 (2020).
- J. Park, S. S. Park, and Y. S. Won, *Electrochim. Acta*, **107**, 467 (2013).
- K. P.-C. Yao, J. S. Okasinski, K. Kalaga, J. D. Almer, and D. P. Abraham, *Adv. Energy Mater.*, **9**, 1803380 (2019).
- C. L. Berhaut, D. Z. Dominguez, P. Kumar, P.-H. Jouneau, W. Porcher, D. Aradilla, S. Tardif, S. Pouget, and S. Lyonard, *ACS Nano*, **13**, 11538 (2019).
- Y. Chen, F. Guo, L. Yang, J. Lu, D. Liu, H. Wang, J. Zheng, X. Yu, and H. Li, *Chinese Phys. B*, **31**, 78201 (2022).
- P.-F. Lory, B. Mathieu, S. Genies, Y. Reynier, A. Boulineau, W. Hong, and M. Chandresris, *J. Electrochem. Soc.*, **167**, 120506 (2020).
- A. Latz and J. Zausch, *J. Power Sources*, **196**, 3296 (2011).
- D. J. Pereira, A. M. Aleman, J. W. Weidner, and T. R. Garrick, *J. Electrochem. Soc.*, **169**, 20577 (2022).
- W. Ai, N. Kirkaldy, Y. Jiang, G. Offer, H. Wang, and B. Wu, *J. Power Sources*, **527**, 231142 (2022).
- X. Gao, S. Li, J. Xue, D. Hu, and J. Xu, *Adv. Energy Mater.*, **13**, 2202584 (2023).
- C. Heubner, T. Liebmann, C. Lämmel, M. Schneider, and A. Michaelis, *J. Power Sources*, **363**, 311 (2017).
- A. Klein, P. Axmann, and M. Wohlfahrt-Mehrens, *J. Electrochem. Soc.*, **163**, A1936 (2016).
- D. P. Finegan et al., *Nano Lett.*, **19**, 3811 (2019).
- J. Moon et al., *Nat. Commun.*, **12**, 2714 (2021).
- K. Richter, T. Waldmann, N. Paul, N. Jobst, R.-G. Scurtu, M. Hofmann, R. Gilles, and M. Wohlfahrt-Mehrens, *ChemSusChem*, **13**, 529 (2020).
- C. Heubner, T. Liebmann, O. Lohrborg, S. Cangaz, S. Maletti, and A. Michaelis, *Batteries & Supercaps*, **5**, e202100182 (2022).
- C. L. Berhaut, M. Miroló, D. Z. Dominguez, I. Martens, S. Pouget, N. Herlin-Boime, M. Chandresris, S. Tardif, J. Drnec, and S. Lyonard, *Adv. Energy Mater.*, **183**, 1 (2023).
- M. Flügel, M. Bolsinger, M. Marinaro, V. Knoblauch, M. Hölzle, M. Wohlfahrt-Mehrens, and T. Waldmann, *J. Electrochem. Soc.*, **170**, 60536 (2023).
- M. Flügel, K. Richter, M. Wohlfahrt-Mehrens, and T. Waldmann, *J. Electrochem. Soc.*, **169**, 50533 (2022).
- Malvern Panalytical, (2017), <https://www.malvernpanalytical.com/en/learn/knowledge-center/Application-notes/an20151201highqualityoperandoxraydiffraction-pouchbaglithiumbatteries>, last checked: 25.08.2023.
- J. Feinauer, T. Brereton, A. Spettl, M. Weber, I. Manke, and V. Schmidt, *Comput. Mater. Sci.*, **109**, 137 (2015).
- Math2Market GmbH, (2023), <https://geodict.com/> GeoDict simulation software last checked on: 09.12.2022 <https://doi.org/10.30423/release.geodict202310.30423/release.geodict2023>.
- ITWM, *BEST - Battery and Electrochemistry Simulation Tool*. (2020), <http://itwm.fraunhofer.de/best>.
- V. de Lauri, L. Krumbain, S. Hein, B. Prifling, V. Schmidt, T. Danner, and A. Latz, *ACS Appl. Energy Mater.*, **4**, 13847 (2021).
- L. S. Kremer, T. Danner, S. Hein, A. Hoffmann, B. Prifling, V. Schmidt, A. Latz, and M. Wohlfahrt-Mehrens, *Batteries & Supercaps*, **3**, 1172 (2020).
- M. Doyle, J. Newman, A. S. Gozdz, C. N. Schmutz, and J. -M. Tarascon, *J. Electrochem. Soc.*, **143**, 1890 (1996).
- N. Ding, J. Xu, Y. X. Yao, G. Wegner, X. Fang, C. H. Chen, and I. Lieberwirth, *Solid State Ionics*, **180**, 222 (2009).
- M. Safari and C. Delacourt, *J. Electrochem. Soc.*, **158**, A562 (2011).
- A. Latz and J. Zausch, *Beilstein J. Nanotechnol.*, **6**, 987 (2015).
- R. Chandrasekaran and T. F. Fuller, *J. Electrochem. Soc.*, **158**, A859 (2011).
- M. Klett, J. A. Gilbert, K. Z. Pupek, S. E. Trask, and D. P. Abraham, *J. Electrochem. Soc.*, **164**, A6095 (2017).
- M. Weiss et al., *Adv. Energy Mater.*, **11**, A1060 (2021).
- S. B. Olou'ou Guifo, J. E. Mueller, D. Henriques, and T. Markus, *Physical Chemistry Chemical Physics: PCCP*, **24**, 9432 (2022).
- V. Zinth, C. von Lüders, M. Hofmann, J. Hattendorff, I. Buchberger, S. Erhard, J. Rebelo-Kornmeier, A. Jossen, and R. Gilles, *J. Power Sources*, **271**, 152 (2014).
- C. von Lüders, V. Zinth, S. V. Erhard, P. J. Osswald, M. Hofmann, R. Gilles, and A. Jossen, *J. Power Sources*, **342**, 17 (2017).
- F. M. Kindermann, A. Noel, S. V. Erhard, and A. Jossen, *Electrochim. Acta*, **185**, 107 (2015).
- D. Rehnlund, F. Lindgren, S. Böhme, T. Nordh, Y. Zou, J. Pettersson, U. Bexell, M. Boman, K. Edström, and L. Nyholm, *Energy Environ. Sci.*, **10**, 1350 (2017).